COMMUNICATIONS PHYSICS

ARTICLE

https://doi.org/10.1038/s42005-020-0351-1 OPEN

Sign changing pairing in single layer FeSe/$SrTiO_3$ revealed by nonmagnetic impurity bound states

Huimin Zhang[1], Zhuozhi Ge[1,2], Michael Weinert[2] & Lian Li[1]✉

The discovery of high-temperature superconductivity in single layer FeSe epitaxially grown on $SrTiO_3$(001) substrates has instigated extensive debate over whether its pairing symmetry is conventional sign-preserving *s*-wave or unconventional sign-changing. Here, we probe the pairing state for single layer FeSe/$SrTiO_3$ grown by molecular beam epitaxy using scanning tunneling microscopy/spectroscopy. We observe robust in-gap bound states induced by nonmagnetic Fe-vacancy defects within the Fe-plane, which exhibit strong spatial electron-hole asymmetry with two-fold symmetry in hole states and four-fold in electron states. The bound states exhibit no energy shift or splitting under an applied magnetic field, consistent with a sign-changing order parameter. This is further confirmed by defect bound state quasiparticle interference that shows a sign-changing behavior with a pair of corresponding peaks at the positive and negative energies near the impurity bound states. Our findings provide unambiguous evidence for a sign-changing pairing symmetry for single layer FeSe/$SrTiO_3$.

[1] Department of Physics and Astronomy, West Virginia University, Morgantown, WV 26506, USA. [2] Department of Physics, University of Wisconsin, Milwaukee, WI 53201, USA. ✉email: lian.li@mail.wvu.edu

The Cooper pairs in a superconductor can be locally broken by impurity scattering, leading to Bogoliubov quasiparticle excitations that can reveal the nature of the superconducting pairing state[1]. For conventional superconductors, only magnetic impurities can break the Cooper pairs, while for unconventional superconductors, both magnetic and non-magnetic impurities can induce such bound states. Hence, probing bound states and quasi-particle scattering at the atomic scale using scanning tunneling microscopy/spectroscopy (STM/S) has been a proven phase-sensitive method for probing pairing symmetry of superconductors. Well known examples include the observation of asymmetric spatial distribution of bound states for electrons and holes in cuprates, which provides unambiguous evidence for $d_{x^2-y^2}$ wave pairing[1–4].

For Fe based superconductors, the determination of pairing symmetry has been challenging due to the multiple bands crossing the Fermi level, giving rise to a number of pairing symmetries[5]. The recent discovery of high-temperature superconductivity in single-layer FeSe epitaxially grown on $SrTiO_3$(001) substrate[6,7] provides a model system to probe the pairing states of Fe-based superconductors. Because of electron doping from the STO substrate[8], the Fermi surface of FeSe/STO consists of only electron pockets at the Brillouin zone (BZ) corner M points, while the hole pockets at Γ point are entirely below the Fermi energy[9,10]. The lack of hole pockets challenges the spin fluctuation picture that involves a sign reversal order parameter between the electron and hole pockets[11,12]. This has instigated extensive debate on the symmetry of pairing state in single-layer FeSe, with leading contender being sign-preserving conventional s-wave pairing[13], and unconventional sign-changing extended s-wave[14,15] and nodeless d-wave pairing[16–19], hence experimental validation are sorely needed[20].

Impurity scattering has been utilized to investigate the superconducting pairing symmetry of single-layer FeSe/STO, however with conflicting results[13,21,22]. A plain s-wave has been suggested in an earlier STM work[13], based on quasiparticle interference off adsorbates on the surface of FeSe, where no impurity-induced bound states were observed for nonmagnetic Zn, Ag, and K adatoms. However, more recent work shows that even for nonmagnetic surface K[21] and Pb adatoms[22], bound states near the superconducting gap edge were found after careful data analysis. The emergence of the induced bound states by these nonmagnetic surface adatoms[21,22] indicates sign-reversing pairing scenarios, challenging the plain s-wave pairing symmetry. One concern for scattering by surface adatoms is that the induced bound states are located near the superconducting gap edges due to weak scattering[23], which may be challenging to discern due to their close proximity to the coherence peaks. As such, the pairing symmetry for single-layer FeSe/STO remains controversial, and unambiguous verification of induced in-gap bound states and quasiparticle scattering off nonmagnetic impurities within the Fe plane is crucial.

In this work, we probe bound states induced by nonmagnetic impurities within the Fe-plane of single-layer FeSe/STO, whose nonmagnetic nature is verified by magnetic field dependent studies. We observe robust in-gap bound states with strong spatial electron-hole asymmetry, which provides clear evidence for sign-changing pairing symmetry. We further carry out systematic impurity scattering studies and apply the recently proposed defect bound state (DBS) quasiparticle interference (QPI) method[24–27] to provide additional support for a sign reversal pairing order parameter, consistent with extended s-wave[14,15] or nodeless d-wave pairing[16].

Results

Non-magnetic defects in single-layer FeSe/STO. Figure 1a shows typical surface morphology of superconducting single-layer FeSe film that is conformal to the step-terrace morphology of the STO substrate. The film is also characterized by a high density of grain boundaries (GBs), appearing as a network of meandering lines with low contrast, similar to previous reports[6,7]. dI/dV spectroscopy reveals a typical "U" shape superconducting gap structure with two coherence peaks, which exhibit spatial variations (Supplementary Fig. 1). Fitting the histogram of the superconducting gaps by Gaussian functions yields an average value of $\Delta_1 = 11.1 \pm 0.1$ meV and $\Delta_2 = 17.5 \pm 0.1$ meV, comparable to previous reports[6,13,21]. The superconducting transition temperature (T_C) is ~60 K from our own angle resolved photoemission spectroscopy (ARPES) measurements[28], comparable to 65 K in previous reports[10].

While defect density on as-grown single-layer FeSe/STO film is low, at $\sim 5.0 \times 10^{11}$ cm^{-2}, higher density ($\sim 1.5 \times 10^{13}$ cm^{-2}) can be introduced by capping the FeSe films with amorphous Se film first, and then annealing to remove the Se layer (Fig. 1b and Supplementary Fig. 2). Five types of defects can be created that are either two- or four-fold symmetric (Supplementary Fig. 3). Accounting for 90% of all defects are of types A and B (Fig. 1c, d), which are centered at the bridge site, i.e., Fe site, of the top-layer Se lattice, and appear as a dumbbell consisting of two bright lobes that are asymmetric in intensity at adjacent Se sites[29,30]. These dumbbell features have been reported in earlier studies and attributed to Fe vacancy and Se_{Fe} substitutional defects. While the nature of the dumbbell defects is still under debate[21,29], comparison between our density functional theory calculations and STM images taken at liquid nitrogen temperature indicates that type A defects are Fe vacancies (Supplementary Fig. 4). In contrast, the four-fold symmetric defects (Supplementary Fig. 3c–e) are located at Se sites, likely Se-site related defects[21], and therefore are not the focus of this work.

dI/dV spectra taken at the center of dumbbell defects show strongly suppressed coherence peaks as well as pronounced resonance peaks inside the superconducting gap, as depicted in Fig. 1e, f. The energy position of bound states for Type A and B defects are −2.7 meV (inside the superconducting gap) and −8.3 meV (near the inner coherence peak), respectively. The resonance peak at the center of the impurity site can be up to three times stronger than the normal state conductance. Magnetic field dependent measurements (Fig. 1e, f) further indicate that while the intensities of these states are slightly suppressed in an external magnetic field; no shift or splitting of these peaks are observed up to 9 T out-of-plane or 2 T in-plane fields, indicating both these types of defects are nonmagnetic.

We have also carried out tunneling spectroscopy measurements at 400 mK with improved energy resolution of 0.36 meV, as determined by measuring the superconducting gap of a well-known superconductor Pb (Supplementary Fig. 5), which should be sufficient to resolve the 1 meV Zeeman splitting that's typical for this material system[31]. Magnetic-field dependent dI/dV spectra of the dumbbell defects taken at this temperature are shown in Supplementary Fig. 6, where again no shifting or splitting of the bound states are observed at ±9 T magnetic field. Note that while some fluctuations in the energy position of the bound state are observed with magnetic field, they are within the spectral energy resolution, and do not show a linear dependence on the magnetic field as would be expected from Zeeman effect. These results unambiguously indicate that the dumbbell defects, both type A and type B, are not magnetic.

We further note that these observations are in marked contrast to magnetic Fe vacancy defects in KFe_2Se_2 films[31], where an energy shift of ~1 meV (at 9 T) is resolved at 400 mK, as well as a

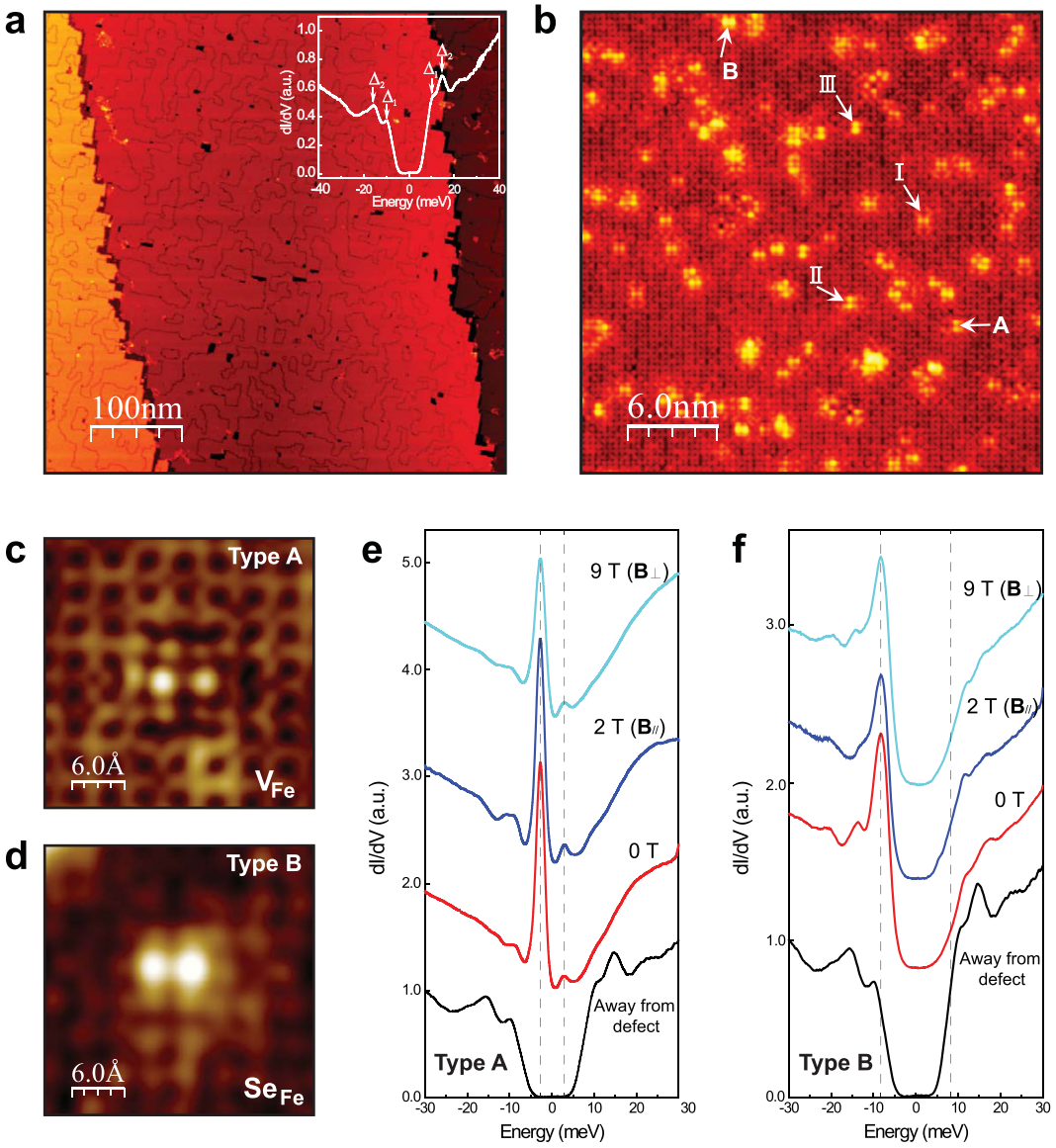

Fig. 1 Surface morphology and defects for single-layer FeSe/STO films. a Scanning tunneling microscopy (STM) topographic image of single-layer FeSe/STO films. Inset: A typical differential conductance (d*I*/d*V*) spectrum measured at 4.3 K away from defects. The two-gap feature is labeled as Δ_1 and Δ_2. **b** Atomic resolution image of various intrinsic defects. Setpoint: Bias (V) = 20 mV, tunneling current (I) = 500 pA. **c**, **d** Close-up atomic resolution images of the type A and B defects labeled in (**b**). Setpoint: V = 30 mV, I = 200 pA. **e**, **f** Magnetic-field-dependent d*I*/d*V* spectra for type A and B defects, respectively. The peak positions of the impurity bound states do not shift or split under an out-of-plane 9 T ($\mathbf{B}_\perp$) or in-plane 2 T ($\mathbf{B}_{//}$) magnetic fields, indicating their non-magnetic nature. The black spectra are measured at regions away from defects, demonstrating a typical double-gap structure. The spectra labeled as 0 T, 2 T ($\mathbf{B}_{//}$) and 9 T ($\mathbf{B}_\perp$) are collected at the defect center in **c**, **d**, which are offset vertically for clarity.

clear linear magnetic field dependence of the energy position of the bound states.

Spatial and energy dependence of bound states. Differential conductance maps of Type A dumbbell defect (Fig. 2a) further reveal that these in-gap bound states are confined to the vicinity of the defects in real space, but do exhibit a different spatial distribution for the electron- and hole-like states. Specifically, the hole-like bound state at −4.4 meV exhibits a two-fold symmetry (Fig. 2b), while the electron-like bound state at +4.4 meV exhibits a four-fold symmetry (Fig. 2c) as schematically shown in Fig. 2d. The intensity for the hole-like bound state is the strongest directly at the impurity site (Fig. 2e). In contrast, the electron-like bound state has the highest intensity at the four lobes, as shown in the d*I*/d*V* spectrum taken at one of the lobes (Fig. 2f). A strong electron-hole asymmetry is clearly seen here where the local maxima and minima occur at different lattice sites with respect to the impurity. A detailed site dependent measurement of the bound states is shown in Supplementary Fig. 7, where the intensity of the hole state decreases from the defect site to the nearest neighbor (NN), next nearest neighbor (NNN), 3rd NN, and so on, while the electron state emerges, with increasing intensity in the reverse order, reaching maximum at 3rd NN. Overall, the spatial distribution at +4.4 meV shows a C_2 symmetry, while at −4.4 meV it is approximately C_4 symmetric. Moreover, the C_2 symmetry is along the dumbbell defect direction (Fig. 2b), whereas the relatively bright four-fold region is along the Fe–Fe direction (Fig. 2c), 45° to the Se–Se lattice, consistent with the C_4 symmetry of the superconducting Fe plane. Similar electron-hole asymmetry is also observed for type B defect, as shown in Supplementary Fig. 8. These observations of the in-gap

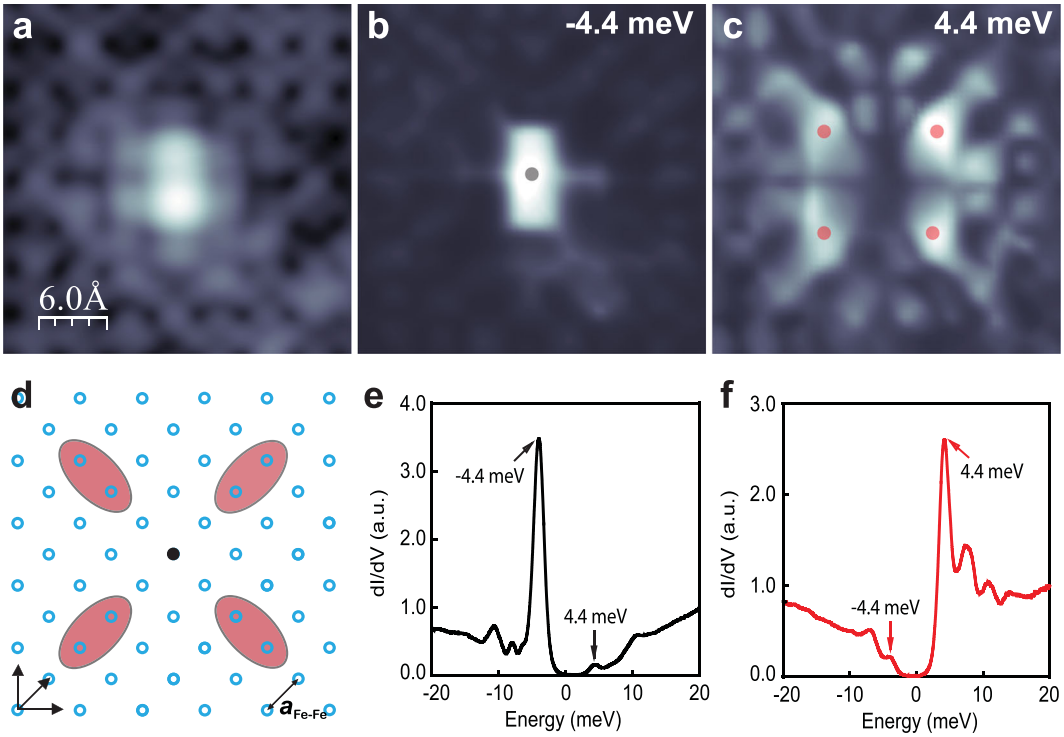

Fig. 2 Spatial distribution of bound states for dumbbell defect A (Fe vacancy). a Topographic image for Type A defect. Setpoint: $V = -30$ mV, $I = 1000$ pA. **b**, **c** Differential conductance maps at −4.4 meV and 4.4 meV, respectively, over the same region in (**a**). Setpoint: $V = 12$ mV, $I = 500$ pA. **d** Schematic representation of the Fe lattice. The distribution of the bound state at positive energy is illustrated by four red ellipses based on conductance map in (**c**). The Fe vacancy defect is labeled by solid black dot in the center. **e** d*I*/d*V* spectrum measured at the defect center (at the gray dot in **b**). **f** d*I*/d*V* spectrum taken at one of the four bright lobes as marked by red dots in (**c**).

bound states and spatial electron-hole asymmetry are similar to those of *d*-wave cuprate superconductors[1–3], indicating an unconventional pairing symmetry in single-layer FeSe/STO. Note that measurements at 77 K indicate that there are no impurity states within ±45 meV of the Fermi level for type A defects (Supplementary Fig. 9b). Furthermore, d*I*/d*V* maps between ±20 meV exhibit no electron-hole asymmetry (Supplementary Fig. 9c–n) in the normal state.

The presence of these defects, however, modifies the normal states around −0.26 eV. For type A, the peak shifts towards the Fermi level by as much as 14 meV (Supplementary Fig. 10b), indicating local hole doping. In contrast, for type B defects, the peak moves away from the Fermi level (Supplementary Fig. 10d), consistent with electron doping[8,32]. Interestingly, these shifts in the normal states are also directly correlated with the energy positions of the bound states. For example, for the three type A defects I, II, and III (marked in Figs. 1b and 3a–c), the bound states shift towards the Fermi level in tandem with the normal state as shown in Fig. 3d, e. Analysis of up to 70 defects indicates that the bound state energy position can vary between −1.7 and −7.5 meV. Plotted in Fig. 3f, g are histogram of the bound states, and the correlation between the normal-state and the bound-state peak energies. While the origin of such correlation is not known at the moment, the normal-state peak energy shifts downward as the bound state shifts towards the superconducting edge, suggesting that local electron doping is one of the possible causes for the energy shift of the bound states. Note that this behavior deviates from that of LiFeAs, where the bound states induced by different impurities are pinned near the coherence peaks[33].

These observations of in-gap bound states induced by non-magnetic impurities within the Fe plane, particularly their spatial electron-hole asymmetry, i.e., a two-fold hole-like state and four-fold electron-like state, are the defining signatures of Bogoliubov quasiparticle excitations. In turn they strongly suggest a sign-changing unconventional order parameter in single-layer FeSe/STO, which is further confirmed by the defect bound state phase-referenced QPI discussed below.

Defect bound state phase-referenced quasiparticle interference. Impurities, particularly those located within the Fe plane such as Fe vacancies can serve as strong scattering centers for quasiparticles and produce standing waves in real space (Fig. 4a), which can be better seen in the energy dependent conductance maps in Fig. 4b–d. Fast Fourier transforms (FFTs) of these conductance maps reveal information in the momentum space that can be understood by comparing to Fermi surface maps obtained from ARPES[9,10], also sketched here in Fig. 4e. Results for three representative energies are shown in Fig. 4f–h, with additional data at other energies between ±20 meV presented in Supplementary Figs. 11 and 12. The FFTs are four-fold symmetrized and subtracted by a 2D-gaussian-function background around Γ point to improve signal-to-noise ratio. Similar to previous reports[13,34], typical nine-ring features in q space are observed, produced by quasiparticle scattering including intra-pocket $\mathbf{q}_1$ and inter-pocket $\mathbf{q}_2$ and $\mathbf{q}_3$ as labeled in Fig. 4f. The scattering rings induced by $\mathbf{q}_2$ and $\mathbf{q}_3$ appear more as arcs, lacking four-fold symmetry, likely related to orbital features[13].

While these FFTs yield the intensities of scattering channels, they do not provide any phase information. For unconventional superconductors with sign change between different Fermi surfaces, additional phase shifts are expected near the bound state induced by nonmagnetic impurities. This phase information can be obtained from the recently developed defect bound states-QPI technique[24–27], where a pair of positive and negative peaks

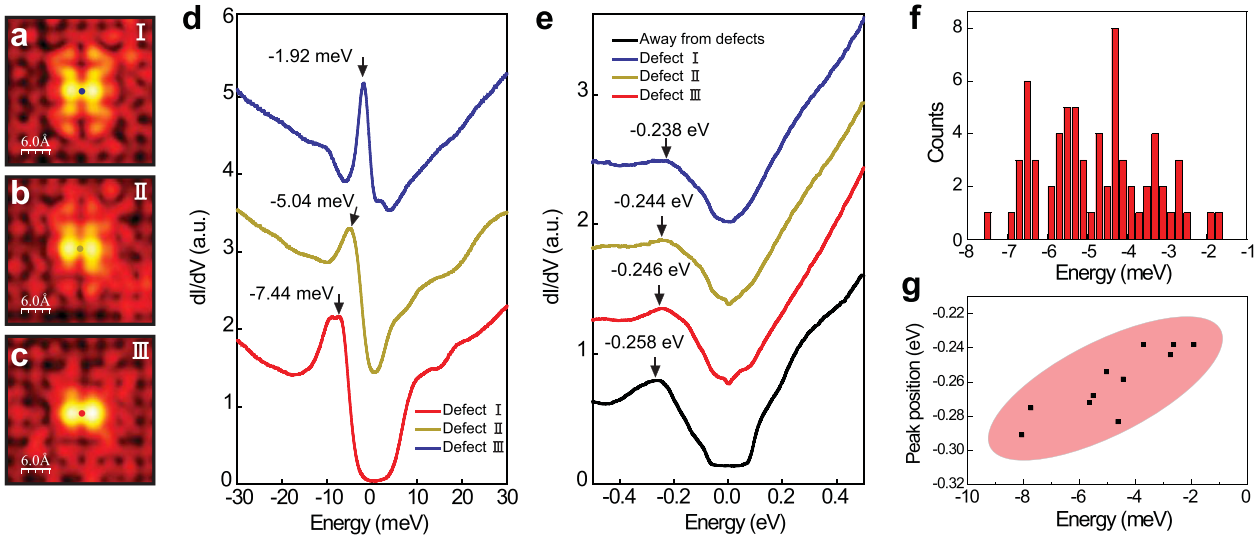

Fig. 3 Correlation between bound state energy and local doping level near dumbbell defects. a–c Topographic images of three Type A defects on single-layer FeSe/STO films, labeled as I, II, and III in Fig. 1b. Setpoint: $V = 20$ mV, $I = 1.0$ nA. **d** dI/dV spectra showing bound states for defects I (−1.92 meV), II (−5.04 meV), and III (−7.44 meV). **e** Larger energy range dI/dV spectra for defects I, II, III, and the region away from the defects, showing that the impurity bound state moves closer to the superconducting edge with more electron doping. **f** Histogram of energies of bound states based on measurements from 70 dumbbell defects. **g** Correlation between the normal-state and bound-state energies.

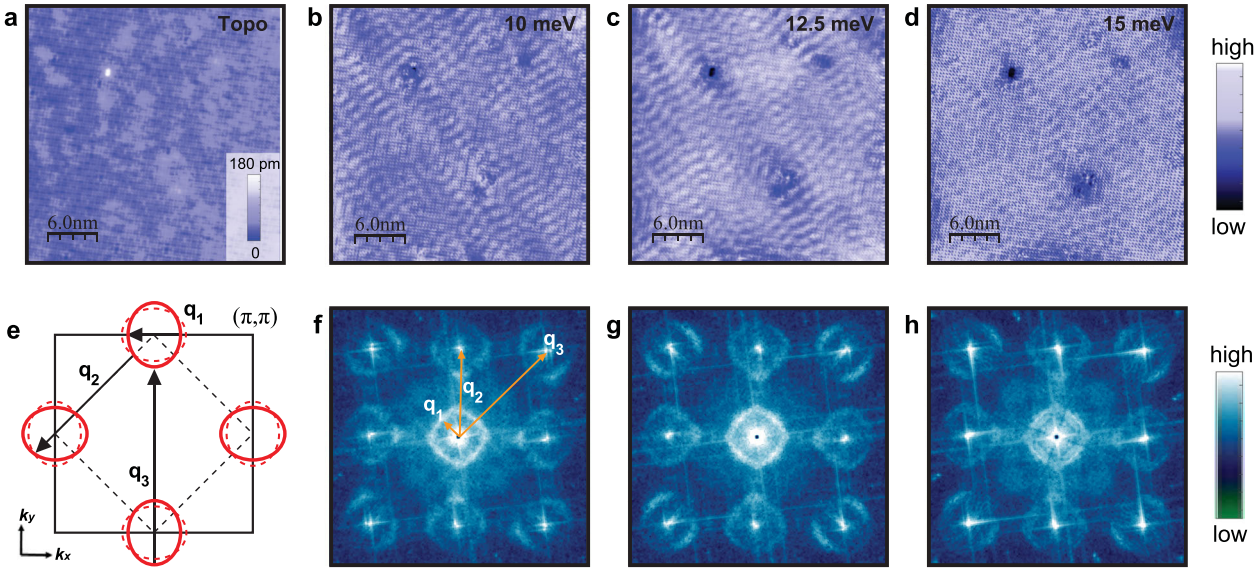

Fig. 4 Differential conductance maps in real space and corresponding quasiparticle interference (QPI) patterns. a Topographic image of a 30 × 30 nm^2 region. Setpoint: $V = 16$ mV, $I = 0.1$ nA. **b–d** Real space differential conductance maps g (**r**, E) in **a** (setpoint: $V = 16$ mV, $I = 0.1$ nA, $V_{rms} = 1$ mV). **e** Schematic of Fermi surface and Fermi pocket scatterings of single-layer FeSe/STO in **k** space. The solid square is the unfolded Brillouin zone (BZ) and the dashed square is the folded BZ. The red solid and dashed ellipses are the electron and folded pockets at BZ corners. The black arrows denote possible scattering vectors $\mathbf{q_1}$, $\mathbf{q_2}$, and $\mathbf{q_3}$. **f–h** Fast Fourier transformation (FFT) of real-space differential conductance maps in (**b–d**), respectively. All the FFTs are four-fold symmetrized and the core center is subtracted by a 2D-gaussian-function background.

are expected to appear in g_{pr} $(q, +E)$ and g_{pr} $(q, -E)$, respectively, at energies near the nonmagnetic impurity bound-state energies $\pm E_B$ (see Methods).

For a type A defect (located at the center of the maps), a series of phase-referenced QPI $g_{pr}(q, E)$ are calculated following Eqs. (1)–(3) (see Methods). Results at ±4.4 meV (bound state energy) and ±10.4 meV (coherence peak of Δ_1) are shown in Fig. 5a–h, with additional data at other energies between ±12 meV presented in Supplementary Figs. 13 and 14. For positive energies (Fig. 5e, f), $g_{pr}(q, E)$ are positive everywhere, as expected. On the other hand, at negative energies (Fig. 5g, h), both positive and negative values are observed. Particularly for $E = -4.4$ meV, the region between the two circles (defined by $0.24\pi/a < \mathbf{q} < 0.64\pi/a$, where a is the Fe–Fe bond length) is overwhelmingly negative, indicating that this pocket contains a sign-reversal inter- or intra-pocket scattering. The extent of this region changes with energy, which can be better illustrated by integrating the signal within the area as a function of energy, as shown in Fig. 5i. Clearly, a positive and negative peak is seen at + and − 4.4 meV, respectively, which are energy positions of the impurity-induced bound states, indicating a sign changing pairing parameter for single-layer FeSe/STO. We note that this defect bound states-QPI method was also applied to $(Li_{1-x}Fe_x)OHFe_{1-y}Zn_ySe$, where a similar conclusion on sign-changing pairing was drawn[26].

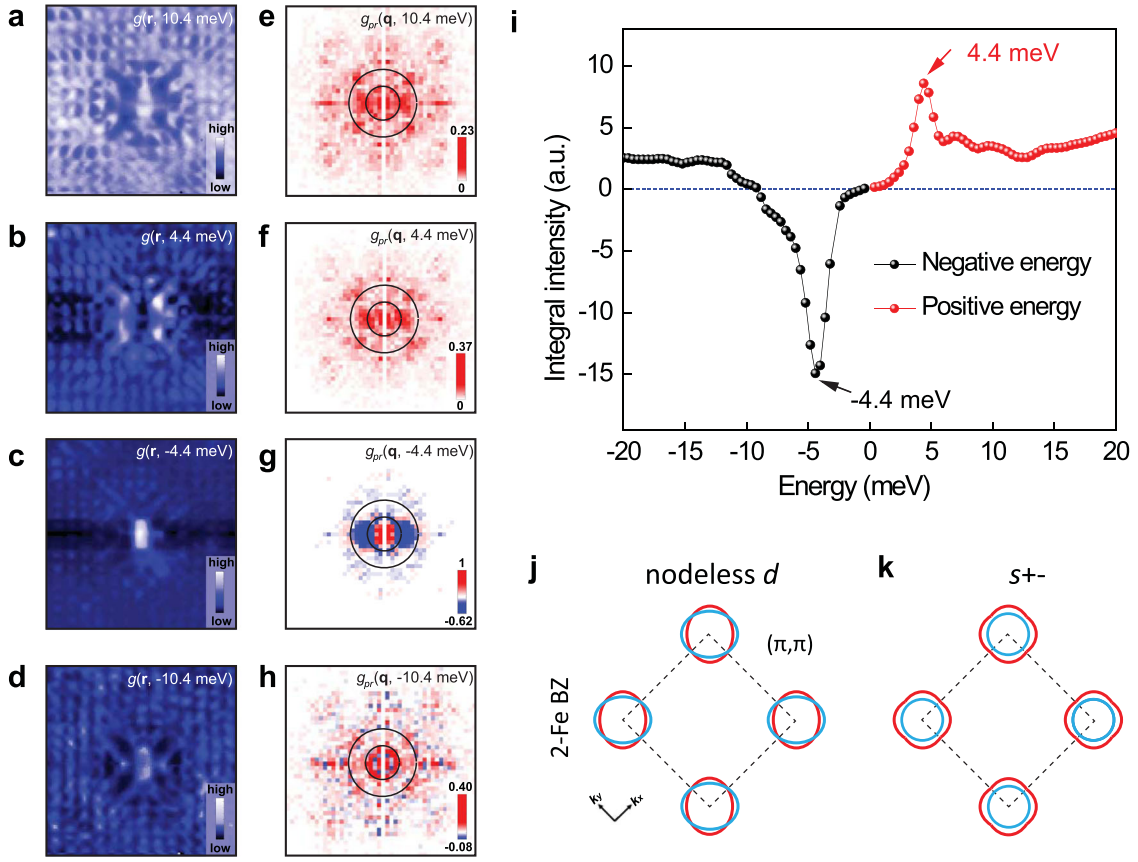

Fig. 5 Phase-referenced defect bound state QPI for single Fe vacancy defect. a–d Real space differential conductance maps g (**r**, E) centered at the Fe vacancy site at 10.4, 4.4, −4.4, and −10.4 meV with single Fe vacancy in the center. Set point: $V = 12$ mV, $I = 0.5$ nA, $V_{rms} = 0.5$ mV. **e–h** Corresponding phase-referenced DBS-QPI patterns g_{pr}(**q**, E). **i** Integrated signals of g_{pr}(**q**, E) as a function of energy. The integrated region is chosen between the two black circles as shown in (**e–h**) with the range of $0.24\pi/a_{\mathrm{Se\text{-}Se}} < \mathbf{q} < 0.64\pi/a_{\mathrm{Se\text{-}Se}}$. The peaks at $-E_B$ and $+E_B$ marked by black and red arrows coincides with the impurity-induced electron-like and hole-like bound states. **j**, **k**, Possible pairing symmetry in single-layer FeSe/STO: nodeless d-wave pairing (**j**) and s_{+-}-wave pairing (**k**). The signs of superconducting gap are shown in red and blue.

The selection of the integrated range is based on the following considerations. First, signals at small **q** are not included as they are usually due to disorder. Second, the integrated regions are carefully determined based on the topography of the Fermi surface. As it is difficult to distinguish $\mathbf{q_1}$ from different scattering channels, the area is selected so that the total signal due to inter- and intra-band large **q**-scattering are all well covered. The integral region is selected as $0.24/a_{Se} < \mathbf{q} < 0.64/a_{Se}$, slight smaller than that of $(Li_{1-x}Fe_x)OHFe_{1-y}Zn_ySe$ ($0.18/a_{Se} < \mathbf{q} < 0.77/a_{Se}$[35] or $0.37/a_{Se} < \mathbf{q} < 0.74/a_{Se}$[26]), due to the smaller electron pockets at M point for single-layer FeSe/STO[36]. Calculations were done for three different integrated areas: $0.24\pi/a < \mathbf{q} < 0.64\pi/a$, $0.32\pi/a < \mathbf{q} < 0.64\pi/a$, and $0.24\pi/a < \mathbf{q} < 0.72\pi/a$, where similar positive and negative peaks are observed at the in-gap bound state energy, only with slight differences in intensity (Supplementary Fig. 15), further demonstrating that the appearances of these peaks are not due to artifacts such as integration areas.

Similar analysis was done for another type A defect with bound states located at ±6.4 meV (Supplementary Fig. 16), as well as a type B defect with bound states at ±9.0 meV (Supplementary Fig. 17), where corresponding positive and negative peaks were also observed, further supporting sign-changing scenarios.

Discussion

Single-layer FeSe/STO only consists of electron pockets at M point and meanwhile, it is fully gapped without nodes. Therefore, the three possible pairing symmetries are plain s-wave, nodeless d-wave, and bonding-antibonding s-wave[20], as summarized in Supplementary Fig. 18. A plain s-wave has been suggested[13] based on quasiparticle interference off adsorbates on the surface of FeSe, where impurity-induced bound states were observed only for magnetic impurities. However, recent work clearly shows that even nonmagnetic surface adsorbates such as K and Pb can induce bound states near the superconducting gap edge[21,22], indicating sign-reversing pairing scenarios. In this work, in-gap bound states from a nonmagnetic impurity within the Fe plane is observed, which exhibit a strong spatial electron-hole asymmetry, also indicating a sign-changing pairing parameter. This is further confirmed by our phase-referenced defect bound state QPI data. Thus, the possibility of plain s-wave can be ruled out, which leaves two scenarios for the pairing symmetry of single-layer FeSe/STO: s_{+-} and nodeless d-wave. However, in both cases, scattering between Fermi surfaces of different orbital character with different signs are possible (Supplementary Fig. 19), and hence cannot be distinguished by this method. Our recent work shows that one-dimensional scattering where the momentum **q** is always perpendicular to edges can provide a means to further differentiate these two pairing scenarios[37].

In conclusion, we systematically studied the in-gap bound states induced by nonmagnetic impurities within the Fe-plane in single-layer FeSe/STO by STM/S. These bound states exhibit a strong spatial electron-hole asymmetry whose energy position is correlated with local doping. We further carried out phase-referenced defect bound state QPI, which reveals corresponding

positive and negative peaks at the bound state energies, indicating a sign change for the order parameter. Our findings provide critical insight into the pairing symmetry of this intriguing high temperature superconductor single-layer FeSe/STO.

Methods

MBE growth and STM/S characterization. Single layer FeSe films were prepared by MBE under Se-rich conditions using high purity Fe (99.995%) and Se (99.9999%) from an e-beam source and a K-cell on the Nb-doped (0.05 wt.%) $SrTiO_3$(001) substrate at 400 °C. The as-grown FeSe films were capped with ~20 nm amorphous Se films, and then transferred in air to a Unisoku-1300 STM system (air exposure time < 15 min), where they were annealed first at 200 °C for 2 h to remove the extra Se and subsequently at between 460 and 480 °C for 1 h to reach superconductivity. Low-temperature STM/S measurements were carried out using a polycrystalline PtIr tip. The STS was acquired by using a lock-in technique with a bias modulation $V_{rms} = 0.5$ mV at 732 Hz, unless otherwise specified.

Defect bound state QPI[24–27]. For $E > 0$, the phase-referenced QPI signals $g_{pr}(\mathbf{q}, E)$ are expressed as

$$g_{pr}(\mathbf{q}, +E) = |g(\mathbf{q}, +E)| \times Re\left[e^{i\left(\theta_{\mathbf{q},+E} - \theta_{\mathbf{q},+E}\right)}\right] = |g(\mathbf{q}, +E)| \quad (1)$$

$$g_{pr}(\mathbf{q}, -E) = |g(\mathbf{q}, -E)| \times Re\left[e^{i\left(\theta_{\mathbf{q},-E} - \theta_{\mathbf{q},+E}\right)}\right] = |g(\mathbf{q}, -E)| \cos\left(\theta_{\mathbf{q},-E} - \theta_{\mathbf{q},+E}\right) \quad (2)$$

The phase term can be expressed as

$$\cos\left(\theta_{\mathbf{q},-E} - \theta_{\mathbf{q},+E}\right) = \cos\theta_{\mathbf{q},-E}\cos\theta_{\mathbf{q},+E} + \sin\theta_{\mathbf{q},-E}\sin\theta_{\mathbf{q},+E} = \frac{Re[g(\mathbf{q}, -E)]}{|g(\mathbf{q}, -E)|}\frac{Re[g(\mathbf{q}, +E)]}{|g(\mathbf{q}, +E)|} + \frac{Im[g(\mathbf{q}, -E)]}{|g(\mathbf{q}, -E)|}\frac{Im[g(\mathbf{q}, +E)]}{|g(\mathbf{q}, +E)|} \quad (3)$$

Here, *Re* denotes the real part of $g(\mathbf{q}, E)$ while *Im* denotes the imaginary part. Based on Eq. (1), $g_{pr}(\mathbf{q}, +E)$ is always positive at positive energy, while at negative energy $g_{pr}(\mathbf{q}, -E)$ is determined by the phase term $\cos(\theta_{\mathbf{q},-E} - \theta_{\mathbf{q},+E})$. If there is a sign change between the initial and final state, the phase shift would be π, hence inducing a negative value since $\cos(\theta_{\mathbf{q},-E} - \theta_{\mathbf{q},+E}) = \cos(\pi) = -1$.

Data availability

The data supporting the findings of this study are available within the paper, its Supplementary Information files, and from the corresponding author upon reasonable request.

Received: 24 June 2019; Accepted: 2 April 2020;
Published online: 07 May 2020

References

1. Balatsky, A. V., Vekhter, I. & Zhu, J.-X. Impurity-induced states in conventional and unconventional superconductors. *Rev. Mod. Phys.* **78**, 373–433 (2006).
2. Pan, S. H. et al. Imaging the effects of individual zinc impurity atoms on superconductivity in $Bi_2Sr_2CaCu_2O_{8+\delta}$. *Nature* **403**, 746–750 (2000).
3. Hudson, E. W. et al. Interplay of magnetism and high-Tc superconductivity at individual Ni impurity atoms in $Bi_2Sr_2CaCu_2O_{8+\delta}$. *Nature* **411**, 920 (2001).
4. Choubey, P., Kreisel, A., Berlijn, T., Andersen, B. M. & Hirschfeld, P. J. Universality of scanning tunneling microscopy in cuprate superconductors. *Phys. Rev. B* **96**, 174523 (2017).
5. Hirschfeld, P. J. Using gap symmetry and structure to reveal the pairing mechanism in Fe-based superconductors. *Comptes Rendus Phys.* **17**, 197–231 (2016).
6. Qing-Yan, W. et al. Interface-induced high-temperature superconductivity in single unit-cell FeSe films on $SrTiO_3$. *Chin. Phys. Lett.* **29**, 037402 (2012).
7. Zhang, W.-H. et al. Direct observation of high-temperature superconductivity in one-unit-cell FeSe films. *Chin. Phys. Lett.* **31**, 017401 (2014).
8. Zhang, H. et al. Origin of charge transfer and enhanced electron–phonon coupling in single unit-cell FeSe films on $SrTiO_3$. *Nat. Commun.* **8**, 214 (2017).
9. Liu, D. et al. Electronic origin of high-temperature superconductivity in single-layer FeSe superconductor. *Nat. Commun.* **3**, 931 (2012).
10. He, S. et al. Phase diagram and electronic indication of high-temperature superconductivity at 65 K in single-layer FeSe films. *Nat. Mater.* **12**, 605–610 (2013).
11. Mazin, I. I., Singh, D. J., Johannes, M. D. & Du, M. H. Unconventional superconductivity with a sign reversal in the order parameter of $LaFeAsO_{1-x}F_x$. *Phys. Rev. Lett.* **101**, 057003 (2008).
12. Kuroki, K. et al. Unconventional pairing originating from the disconnected Fermi surfaces of superconducting $LaFeAsO_{1-x}F_x$. *Phys. Rev. Lett.* **101**, 087004 (2008).
13. Fan, Q. et al. Plain s-wave superconductivity in single-layer FeSe on $SrTiO_3$ probed by scanning tunnelling microscopy. *Nat. Phys.* **11**, 946–952 (2015).
14. Mazin, I. I. Symmetry analysis of possible superconducting states in $K_xFe_ySe_2$ superconductors. *Phys. Rev. B* **84**, 024529 (2011).
15. Khodas, M. & Chubukov, A. V. Interpocket pairing and gap symmetry in Fe-based superconductors with only electron pockets. *Phys. Rev. Lett.* **108**, 247003 (2012).
16. Agterberg, D. F., Shishidou, T., O'Halloran, J., Brydon, P. M. R. & Weinert, M. Resilient nodeless d-wave superconductivity in monolayer FeSe. *Phys. Rev. Lett.* **119**, 267001 (2017).
17. Maier, T. A., Graser, S., Hirschfeld, P. J. & Scalapino, D. J. d-wave pairing from spin fluctuations in the $K_xFe_{2-y}Se_2$ superconductors. *Phys. Rev. B* **83**, 100515 (2011).
18. Wang, F. et al. The electron pairing of $K_xFe_{2-y}Se_2$. *EPL Europhys. Lett.* **93**, 57003 (2011).
19. Kreisel, A. et al. Orbital selective pairing and gap structures of iron-based superconductors. *Phys. Rev. B* **95**, 174504 (2017).
20. Huang, D. & Hoffman, J. E. Monolayer FeSe on $SrTiO_3$. *Annu. Rev. Condens. Matter Phys.* **8**, 311–336 (2017).
21. Liu, C. et al. Extensive impurity-scattering study on the pairing symmetry of monolayer FeSe films on $SrTiO_3$. *Phys. Rev. B* **97**, 024502 (2018).
22. Liu, C. et al. Spectroscopic imaging of quasiparticle bound states induced by strong nonmagnetic scatterings in one-unit-cell FeSe/$SrTiO_3$. *Phys. Rev. Lett.* **123**, 036801 (2019).
23. Chen, X., Mishra, V., Maiti, S. & Hirschfeld, P. J. Effect of nonmagnetic impurities on $s_\pm$ superconductivity in the presence of incipient bands. *Phys. Rev. B* **94**, 054524 (2016).
24. Chi, S. et al. Determination of the superconducting order parameter from defect bound state quasiparticle interference. Preprint at https://arxiv.org/abs/1710.09089 (2017).
25. Chi, S. et al. Extracting phase information about the superconducting order parameter from defect bound states. Preprint at https://arxiv.org/abs/1710.09088 (2017).
26. Gu, Q. et al. Sign-reversal superconducting gaps revealed by phase-referenced quasiparticle interference of impurity-induced bound states in $Li_{1-x}Fe_xOHFe_{1-y}Zn_ySe$. *Phys. Rev. B* **98**, 134503 (2018).
27. Chen, M. et al. Direct visualization of sign-reversal $s_\pm$ superconducting gaps in $FeTe_{0.55}Se_{0.45}$. *Phys. Rev. B* **99**, 014507 (2019).
28. Yang, M., Yan, C., Ma, Y., Li, L. & Cen, C. Light induced non-volatile switching of superconductivity in single layer FeSe on $SrTiO_3$ substrate. *Nat. Commun.* **10**, 1–7 (2019).
29. Huang, D. et al. Dumbbell defects in FeSe films: A scanning tunneling microscopy and first-principles investigation. *Nano Lett.* **16**, 4224–4229 (2016).
30. Choubey, P., Berlijn, T., Kreisel, A., Cao, C. & Hirschfeld, P. J. Visualization of atomic-scale phenomena in superconductors: application to FeSe. *Phys. Rev. B* **90**, 134520 (2014).
31. Li, W. et al. Phase separation and magnetic order in K-doped iron selenide superconductor. *Nat. Phys.* **8**, 126–130 (2012).
32. Tang, C. et al. Superconductivity dichotomy in K-coated single and double unit cell FeSe films on $SrTiO_3$. *Phys. Rev. B* **92**, 180507 (2015).
33. Chi, S. et al. Impact of iron-site defects on superconductivity in LiFeAs. *Phys. Rev. B* **94**, 134515 (2016).
34. Huang, D. et al. Revealing the empty-state electronic structure of single-unit-cell FeSe/$SrTiO_3$. *Phys. Rev. Lett.* **115**, 017002 (2015).
35. Du, Z. et al. Sign reversal of the order parameter in $(Li_{1-x}Fe_x)OHFe_{1-y}Zn_ySe$. *Nat. Phys.* **14**, 134–139 (2017).
36. Zhao, L. et al. Common electronic origin of superconductivity in (Li,Fe) OHFeSe bulk superconductor and single-layer FeSe/$SrTiO_3$ films. *Nat. Commun.* **7**, 10608 (2016).
37. Ge, Z. et al. Evidence for d-wave superconductivity in single layer FeSe/$SrTiO_3$ probed by quasiparticle scattering off step edges. *Nano Lett.* **19**, 2497–2502 (2019).

Acknowledgements

Research supported by the U.S. Department of Energy, Office of Basic Energy Sciences, Division of Materials Sciences and Engineering under Award DE-SC0017632.

Author contributions

H.Z. and L.L. conceived the research. Z.G. prepared single-layer FeSe/STO films by MBE. H.Z. carried out the low temperature STM/S measurements. M.W. carried out DFT calculations. H.Z. and L.L. analyzed the data and wrote the paper. All authors discussed the results and commented on the paper.

Competing interests
The authors declare no competing interests.

Additional information
Supplementary information is available for this paper at https://doi.org/10.1038/s42005-020-0351-1.

Correspondence and requests for materials should be addressed to L.L.

Reprints and permission information is available at http://www.nature.com/reprints

Publisher's note Springer Nature remains neutral with regard to jurisdictional claims in published maps and institutional affiliations.

Open Access This article is licensed under a Creative Commons Attribution 4.0 International License, which permits use, sharing, adaptation, distribution and reproduction in any medium or format, as long as you give appropriate credit to the original author(s) and the source, provide a link to the Creative Commons license, and indicate if changes were made. The images or other third party material in this article are included in the article's Creative Commons license, unless indicated otherwise in a credit line to the material. If material is not included in the article's Creative Commons license and your intended use is not permitted by statutory regulation or exceeds the permitted use, you will need to obtain permission directly from the copyright holder. To view a copy of this license, visit http://creativecommons.org/licenses/by/4.0/.

© The Author(s) 2020